THE ORIENTATIONAL RELAXATION OF BIPOLAR ACTIVE REGIONS

Dana Longcope
Department of Physics, Montana State University, Bozeman, MT 59717, USA

Arnab Rai Choudhuri
Department of Physics, Indian Institute of Science, Bangalore 560012, India

August 2, 2001

Abstract. In the mean, bipolar active regions are oriented nearly toroidally, according to Hale's polarity law, with a latitude-dependent tilt known as Joy's Law. The tilt angles of individual active regions deviate from this mean behavior and change over time. It has been found that on average the change is toward the mean angle at a rate characteristic of 4.37 days (Howard, 1996). We show that this orientational relaxation is consistent with the standard model of flux tube emergence from a deep dynamo layer. Under this scenario Joy's law results from the Coriolis effect on the rising flux tube (D'Silva and Choudhuri, 1993), and departures from it result from turbulent buffeting of the tubes (Longcope and Fisher, 1996). We show that relaxation toward Joy's angle occurs because the turbulent perturbations relax on shorter time scales than the perturbations from the Coriolis force. The turbulent perturbations relax more rapidly because they are localized to the topmost portion of the convection zone while the Coriolis perturbations are more widely distributed.

If a fully-developed active region remains connected to the strong toroidal magnetic field at the base of the convection zone, its tilt will eventually disappear, leaving it aligned perfectly toroidally. On the other hand, if the flux becomes disconnected from the toroidal field the bipole will assume a tilt indicative of the location of disconnection. We compare models which are connected and disconnected from the toroidal field. Only those disconnected at points very deep in the convection zone are consistent with observed time scale of orientational relaxation.

1. Introduction

It was pointed out by Hale *et al.* (1919) that bipolar active regions on the solar surface generally appear tilted with respect to the east-west line and this tilt angle θ increases with latitude. More recent studies have confirmed this tendency, known as "Joy's law", in an average sense, although considerable scatter exists around the average (Wang and Sheeley, 1989; Howard, 1992). Bipolar active regions are believed to be produced by magnetic flux rising due to magnetic buoyancy. The flux tubes presumably originate in the tachocline at the base of the convection zone, where the concentrated gradient of rotation produces the strong toroidal magnetic field. Emergence models show that the Coriolis force affects flux tubes rising through the solar convection zone (Choudhuri and Gilman, 1987; Choudhuri, 1989), deflecting an initially toroidal (East-West) flux tube to an angle in quantitative agreement with Joy's law (D'Silva and Choudhuri, 1993; Fan, Fisher, and DeLuca, 1993; D'Silva and Howard, 1993; Fan, Fisher, and McClymont, 1994; Caligari, Moreno-Insertis, and Schüssler, 1995). The interaction of the flux tube with the surrounding turbulence during its rise (Longcope and Fisher, 1996) leads to the random scatter on top of the systemic tilt of Joy's law.

© 2001 *Kluwer Academic Publishers. Printed in the Netherlands.*

Perhaps the best observational evidence for Joy's law and its corollaries has come from the Mount Wilson digitized sunspot data set (Howard, Gilman, and Gilman, 1984) spanning the years 1917-1985. These data contain the locations of multi-spot groups, from which it is possible to calculate the tilt angles θ for an enormous number of bipolar active regions. Howard (1996) went further, to measure the change in tilt angle $\dot{\theta}$ from a subset of 24,597 spot-groups by observing the same region on successive days. A plot of $\dot{\theta}$ against θ, reproduced here in Figure 1, shows a relation between the change and the tilt angle itself.

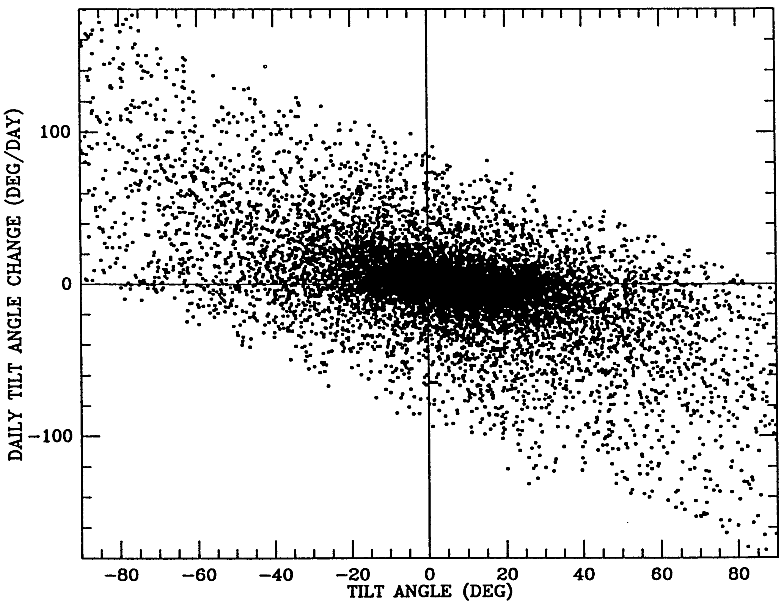

Figure 1. The plot of $\dot{\theta}$ versus θ measured in 24,597 multi-spot sunspot groups in the Mount Wilson digitized sunspot data set. Reproduced from Howard (1996).

The data points in Figure 1 forms a diagonal band whose vertical extent is a tilt angle change of approximately 180 degrees per day. This diagonal trend is an artifact arising from a 180° ambiguity in measurements of θ from sunspot data, which naturally lacks magnetic information. There is a genuine trend in that data within the dense central concentration of points, unaffected by ambiguity. Howard quantified this relationship by plotting the mean tilt angle change in each 5° bin inside the central region $-50^\circ \le \theta \le +50^\circ$ and $-40 \le \dot{\theta} \le +40$ (Figure 4 in Howard 1996). This exhibits an extremely well defined linear trend with slope -0.229 ± 0.004 day^{-1} and intersecting $\dot{\theta} = 0$ at an angle of $\theta = 5.65 \pm 0.32$ degrees. Significantly, this angle of intersection is close to the average tilt angle for sunspot groups according to Joy's law.

From this remarkable data set, Howard concluded that each bipole relaxes from its initial orientation toward the angle θ_J specified by Joy's law. The value of the slope, therefore, gives the time scale on which this relaxation occurs: about 4.37 days. Howard attributes this relaxation to magnetic tension, which would imply that the tube is anchored at the angle θ_J. This interpretation is supported by the fact that smaller active regions rotate faster than larger active regions (Section 3.5 of Howard, 1996).

The plot of $\dot{\theta}$ against θ for the 24,597 multi-spot groups undoubtedly has significance for models of flux tube dynamics, which we wish to further explore in this paper. At the first sight, Howard's interpretation that the tension force causes bipoles to relax from their initial tilt angle θ_0 toward Joy's law angle θ_{J} seems to cast serious doubt on the current picture of emergence, as he himself points out. According to the current picture, Joy's law arises from the Coriolis force. Since this force operates only when the tube rises and disappears after emergence, the persistent relaxation toward θ_{J} after emergence cannot be attributed to the Coriolis force. This implies that another force might be responsible for Joy's law.

This interpretation raises the question of whether a fully-developed active region still remains anchored to the strong toroidal field at the base of the convection zone. If this were so, then magnetic tension would seek to align the bipolar active region eventually in the East-West direction. The time scale for this, however, would be several weeks, which is the time required for magnetic stress to communicate from the bottom of the convection zone to the top as Alfvén waves. A tendency for bipolar regions to align in the east-west direction has not yet been reported, although we shall argue later that Howard's data (Howard, 1996) cannot be used as evidence against it.

If it were found that active regions never relax to an East-West orientation then something must be countering the magnetic tension force from the bottom of the convection zone. One possibility is that bipolar active regions decay before magnetic tension had time to act. Another possibility is that the active region's field has become effectively detached from the bottom of the convection zone. Fan, Fisher, and McClymont (1994) argued that when hydrostatic equilibrium was established in the flux tube's interior it would suffer "dynamic disconnection". This is a state in which the equilibrium magnetic field at some region below the surface is so weak that convective turbulence dominates the flux tube. Dynamic disconnection would prevent magnetic tension from aligning the upper parts of the flux tube in the East-West direction. The observed advection and diffusion of photospheric flux might be manifestation of dynamic disconnection. For the magnetic flux in a decaying active region to spread around and be carried by meridional flow to higher latitudes (Wang, Nash, and Sheeley, 1989; Choudhuri and Dikpati, 1999), it is presumably necessary for the flux to be disconnected from the the base of the convection zone (Spruit, Title, and van Ballegooijen, 1987). In spite of this evidence, very little is known about the process of dynamic disconnection, and no dynamic flux tube model has ever been proposed which uses it.

In this work, we contend that the very short (4.37 days) relaxation time found from fitting $\dot{\theta}$ to θ means that Howard's data probably sheds no light on the extent to which a flux tube is truly anchored. Simple estimates, given below, suggest that in the relaxation time of 4.37 days, information propagating at the Alfvén speed can reach only half the depth of the convection zone, or less. The time scale found in the data points to an effect produced in the upper portion of the flux tube, far from locations of anchoring.

We propose here that Howard's data are, in fact, consistent with the prevailing picture of flux tube dynamics. According to the prevailing picture, both Joy's law and the statistical departures to it arise from perturbations to a toroidal flux tube rising on the surface of a cone of constant latitude. The Coriolis effect on the rising tube introduce a long wavelength perturbation out of this cone, giving rise to Joy's law. Turbulent motions in the upper convection zone introduce shorter wavelength perturbations onto the flux tube, which lead to random departures from Joy's law. After emergence, both the Coriolis force and the coupling to turbulence vanish, and all perturbations relax by magnetic tension. The key to our argument is that the long and short wavelength perturbations relax at different rates. When this simple picture is used to predict $\dot{\theta}$ versus θ in a large sample of model active regions, the data show a steep slope with an intercept at $\theta \simeq \theta_{\mathrm{J}}$, in agreement with Howard's observations. The non-zero intercept arises because the random, short wavelength perturbations are relaxing rapidly toward a value set by the long wavelength perturbation. Thus, Howard's data are consistent with the Coriolis effect as the origin of Joy's law, as well as with convective turbulence as the origin of statistical departures from it.

We demonstrate this interpretation using a simple model of a rising flux tube with small perturbations. The next section reviews the structure of the convection zone, and argues that turbulent perturbations will occur only within its uppermost layers. In Section 3, we derive model equations for the dynamics of a flux tube. In these equations the dynamics transverse to the tube's rise plane (i.e. the plane containing the initial flux tube and the vertical direction) decouple from the other components. After the flux tube has fully emerged, the transverse dynamics describe the perturbations propagating along the tube as kink waves. The orientational relaxation of some simple configurations are presented in Section 4, showing how it relates to tilt angle changes. This model is applied to a statistical data set in Section 5, where we also present a comparison between theoretically synthesized data (by Monte Carlo technique) and observational data. The effect of dynamic disconnection is investigated in Section 6. Our conclusions with suggestions for further work are finally summarized in Section 7.

2. The site of turbulent perturbation

Magnetic flux tubes must rise through the convection zone as reasonably coherent structures in order that the emerging flux be organized as active regions on the solar surface. The flux tubes can resist significant distortion by turbulence only if their internal magnetic energy density is larger than the kinetic energy density of the turbulence. By comparing these energy densities we can ascertain those depths at which we expect turbulent distortions to occur.

The convection zone model of Spruit (1974) provides an estimate of the kinetic energy density $\frac{1}{2}\rho v^2$ in convective turbulence as a function of depth.

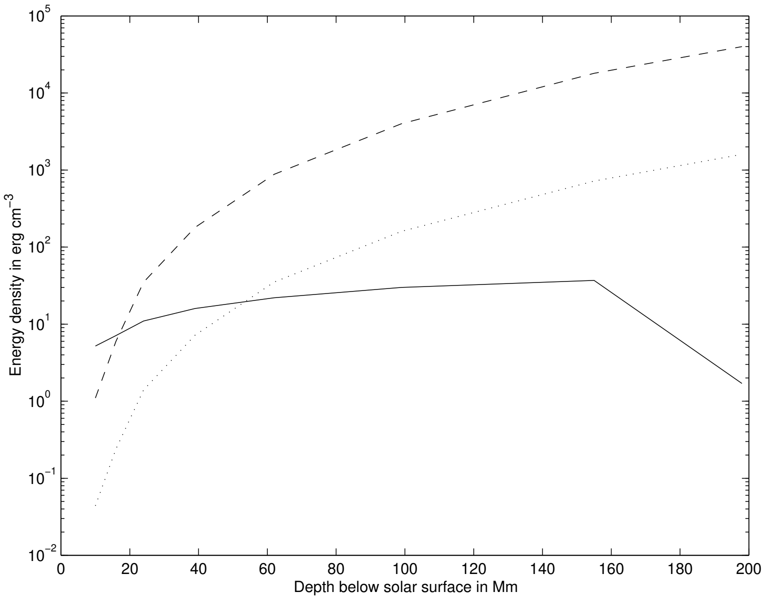

Figure 2. Variation of energy density with depth for a rising flux tube. Solid line: the energy density of surrounding turbulence. Dashed line: the energy density inside a rising flux tube starting with initial magnetic field $B_0 = 10^5$ G. Dotted line: the energy density inside a rising flux tube starting with $B_0 = 2 \times 10^4$ G.

Figure 2 shows that kinetic energy density varies little within the convection zone. While the mass density increases with depth, the turbulent velocity decreases to approximately compensate.

The magnetic energy density inside a flux tube depends on its evolution during rise. An estimate of the field strength can be made using the simplifying assumption that the flux tube rises radially in the form of an axi-symmetric ring. Under this assumption the magnetic field at radius r can be expressed

$$B = B_0 \frac{\rho}{\rho_0} \frac{r}{r_0} \quad , \tag{1}$$

where B_0 and ρ_0 are the magnetic field strength and mass density at the base of the convection zone $r = r_0$. Various simulations of flux tube rise through the convection zone (D'Silva and Choudhuri, 1993; Fan, Fisher, and DeLuca, 1993; D'Silva and Howard, 1993; Fan, Fisher, and McClymont, 1994; Caligari, Moreno-Insertis, and Schüssler, 1995; Longcope and Fisher, 1996) suggest that the surface observations of active regions are best matched by B_0 in the range 50–100 kG. Figure 2 shows the magnetic energy $B^2/8\pi$ versus depth for a symmetric flux ring with initial magnetic field $B_0 = 100$ kG. For the sake of comparison, we also show a tube with the rather low value $B_0 = 20$ kG. It is clear from Figure 2 that the magnetic energy remains higher than the turbulent kinetic energy until the top 30 or 40 Mm of the convection zone. Only within this top portion is the magnetic energy density low enough for the flux tube to be disturbed by turbulence.

We expect that the magnetic field would be stronger under more realistic models for the rise evolution than it is for a symmetric ring. In a symmetric ring the field strength decreases by a factor of ~ 30 by a depth of 24 Mm. From an initial magnetic field strength of $B_0 = 100$ kG, it will fall to 2950 G, comparable to that observed in sunspots. If the tube rises as an Ω-loop rather than a ring, fluid will drain from the its apex (Choudhuri, 1989; D'Silva and Choudhuri, 1993) strengthening the magnetic fields there. Since the axi-symmetric ring model underestimates the field strength, its prediction of the turbulent distortion depth should be considered an upper bound. It is more likely that a rising flux tube is not significantly distorted by the action of turbulence until it reaches depths of 20 to 30 Mm from the solar surface. We will hereafter refer to this as the *turbulent distortion depth* for a flux tube.

Since the flux tube is unaffected by turbulence over at least 80% of its total rise distance, we expect simulations based on thin flux tubes rising through a stationary atmosphere (D'Silva and Choudhuri, 1993; Fan, Fisher, and DeLuca, 1993; Caligari, Moreno-Insertis, and Schüssler, 1994) to provide a reasonable description of their evolution. We therefore expect that the upper part of the flux tube will be inclined in accordance with Joy's law by the time its apex reaches a depth of 40 Mm. The turbulent distortion leading to statistical departures from Joy's law will then occur during its rise through the remaining portion of the convection zone.

The thin flux tube equations will be used in our analysis. This model assumes that the cross-section of the flux tube is smaller than the various scale-heights of the surrounding atmosphere. This should be the case below the uppermost layers of the convection zone. In the regions very close to the solar surface we expect departures from thin flux tube dynamics. In view of the immense complexities of applying the full MHD equations to this problem, we nevertheless apply the thin flux tube equations throughout our calculations.

3. Mathematical formulation

3.1. Thin flux tube dynamics

Dynamical equations for the evolution of a thin flux tube were proposed by Spruit (1981) and have been refined and extended by subsequent authors (Choudhuri, 1990; Cheng, 1992; Moreno-Insertis, Schüssler, and Ferriz-Mas, 1996). The axis of the tube is a space-curve $\mathbf{r}(s,t)$ parameterized by length coordinate s. The velocity $\mathbf{v}(s,t)$ of the material point at coordinate s changes due to the forces of gravity, magnetic tension and aerodynamic drag. The resulting equation governing the evolution of a thin flux tube is (see, for example, Fan, Fisher, and DeLuca, 1993)

$$\frac{d\mathbf{v}}{dt} = \frac{\delta\rho}{\rho}\mathbf{g} + \frac{B^2}{4\pi\rho}\mathbf{k} + \frac{1}{4\pi\rho}\frac{\partial B^2}{\partial s}\,\hat{\mathbf{s}} - 2\boldsymbol{\omega}\times\mathbf{v} + \mathbf{a}_{\mathrm{d}} \quad , \qquad (2)$$

where $\boldsymbol{\omega}$ is the solar rotation vector, and $\mathbf{g}$ is the gravitational acceleration. The Lagrangian time derivative $d/dt = \partial/\partial t + v_s\partial/\partial s$ follows the motion of an element within the tube. The difference between mass density inside and outside the tube, termed over-density $\delta\rho \equiv \rho - \rho^e$, is negative in a buoyant flux tube and will be assumed very small compared to either density. The tangent unit-vector $\hat{\mathbf{s}}$ and curvature vector $\mathbf{k}$ are first and second derivatives of the axis curve

$$\hat{\mathbf{s}} \equiv \frac{\partial \mathbf{r}}{\partial s} \quad , \quad \mathbf{k} \equiv \frac{\partial^2 \mathbf{r}}{\partial s^2} \quad .$$

An effect known as enhanced inertia is frequently included in the perpendicular dynamics of a flux tube (Spruit, 1981). This effect is well known in the two-dimensional Euler equation but its application to the dynamics of a general string in a rotating reference frame is still somewhat controversial (Moreno-Insertis, Schüssler, and Ferriz-Mas 1996; Achterberg, 1996). Since the effect is not crucial to our investigation of tilt angle relaxation, and it complicates the analysis considerably, we have chosen to neglect it in Equation (2).

The tube experiences aerodynamic drag as its axis moves through the external medium with a turbulent velocity $\mathbf{v}^{\mathrm{e}}(\mathbf{r}, t)$. At high Reynolds number, the aerodynamic drag term takes the form (Fan, Fisher, and DeLuca, 1993)

$$\mathbf{a}_{\mathrm{d}} = -\frac{C_{\mathrm{D}}}{2\pi a} |\mathbf{v}_{\perp} - \mathbf{v}^{\mathrm{e}}_{\perp}| (\mathbf{v}_{\perp} - \mathbf{v}^{\mathrm{e}}_{\perp}) \quad , \tag{3}$$

where $\mathbf{v}_{\perp}$ and $\mathbf{v}^{\mathrm{e}}_{\perp}$ are the components of $\mathbf{v}$ and $\mathbf{v}^{\mathrm{e}}$ perpendicular to the axis (i.e. perpendicular to $\hat{\mathbf{s}}$), and C_{D} is the drag coefficient. Assuming a perfectly circular cross-section, the radius is $a(s) = \sqrt{\Phi/\pi B(s)}$.

We shall assume that the turbulent velocity is much smaller than the tube's rise speed $|\mathbf{v}^{\mathrm{e}}| \ll |\mathbf{v}|$ so that the effect of turbulence may be treated perturbatively. This assumption makes it possible to expand (3) as

$$\mathbf{a}_{\mathrm{d}} \simeq -\frac{C_{\mathrm{D}}}{2\pi a} |\mathbf{v}_{\perp}| \mathbf{v}_{\perp} + \frac{C_{\mathrm{D}}}{2\pi a} |\mathbf{v}_{\perp}| \left(\mathbf{I} + \frac{\mathbf{v}_{\perp}\mathbf{v}_{\perp}}{|\mathbf{v}_{\perp}|^2} \right) \cdot \mathbf{v}^{\mathrm{e}}_{\perp} \quad , \tag{4}$$

where I is the identity matrix. We shall further assume that the Coriolis term $-2\boldsymbol{\omega} \times \mathbf{v}$ is a small perturbation to the tube's dynamics. To lowest order, the governing equation for the rising flux tube is

$$\frac{d\mathbf{v}_0}{dt} = \frac{\delta\rho}{\rho}\mathbf{g} + \frac{B^2}{4\pi\rho}\mathbf{k}_0 + \frac{1}{4\pi\rho}\frac{\partial B^2}{\partial s_0}\hat{\mathbf{s}}_0 \quad . \tag{5}$$

If the gravitational vector $\mathbf{g}(s)$ along the entire tube lies in a plane, then the tube's axis will always lie in that same plane. To take advantage of this simplification, we shall neglect the solar curvature and use Cartesian coordinates in which $\mathbf{g} = -g\hat{\mathbf{z}}$ and the initial tube is a straight line along the x axis. In these coordinates there is no source for v_y in the zeroth-order equations and the tube rises purely in the x–z plane, which represents a cone of constant latitude in the solar interior. This nonlinear equation, along with thermodynamic equations and perpendicular pressure balance governing ρ and B, describes the rise of a buoyant flux tube unaffected by the Coriolis effect or external turbulence.

The Coriolis effect and turbulence enter at the next order of our expansion, resulting in a perturbation $\mathbf{r}_1(s, t)$ to the tube's axis. The out-of-plane component, $y_1(s, t)$, solves a linear equation decoupled from the other components. Taking the $\hat{\mathbf{y}}$ component of (2) to leading order gives

$$\frac{d^2 y_1}{dt^2} + \gamma \frac{dy_1}{dt} - \frac{1}{4\pi\rho_0}\frac{\partial}{\partial s_0}\left(B_0^2 \frac{\partial y_1}{\partial s_0}\right) = \gamma v_y^{\mathrm{e}} + 2\mathbf{v}_0 \cdot (\boldsymbol{\omega} \times \hat{\mathbf{y}}) \ , \qquad (6)$$

where s_0 refers to the length along the zeroth-order axis and

$$\gamma(s_0, t) \equiv \frac{C_{\mathrm{D}} |\mathbf{v}_{\perp,0}|}{2\pi a_0} \ , \qquad (7)$$

is a damping frequency due to aerodynamic drag. The Lagrangian time derivatives follow the fluid elements of the unperturbed (zeroth order) tube.

3.2. The tilt relaxation problem

In order to treat the problem of tilt relaxation, we apply the above model in two phases: rise and relaxation. During the rise phase, the evolution of the flux tube in the x–z plane is given by (5). The horizontal perturbations can be found from (6) by separately following the contributions from Coriolis force and turbulence, described by $y_1^{(\mathrm{c})}(s,t)$ and $y_1^{(\mathrm{t})}(s,t)$:

$$\frac{d^2 y_1^{(\mathrm{c})}}{dt^2} + \gamma \frac{dy_1^{(\mathrm{c})}}{dt} - \frac{1}{4\pi\rho_0}\frac{\partial}{\partial s_0}\left(B_0^2 \frac{\partial y_1^{(\mathrm{c})}}{\partial s_0}\right) = 2\mathbf{v}_0 \cdot (\boldsymbol{\omega} \times \hat{\mathbf{y}}) \ , \qquad (8)$$

$$\frac{d^2 y_1^{(\mathrm{t})}}{dt^2} + \gamma \frac{dy_1^{(\mathrm{t})}}{dt} - \frac{1}{4\pi\rho_0}\frac{\partial}{\partial s_0}\left(B_0^2 \frac{\partial y_1^{(\mathrm{t})}}{\partial s_0}\right) = \gamma\, v_y^{\mathrm{e}}(s,t) \ . \qquad (9)$$

The tube is initially toroidal so that $y_1^{(\mathrm{c})}(s,0) = y_1^{(\mathrm{t})}(s,0) = 0$. The source term for (9) is a random function of s and t representing the driving by the local turbulence field through which the flux tube rises. The solution, $y_1^{(\mathrm{t})}(s,t)$ will likewise be a random function.

The source of (8) is the Coriolis effect, whose dependence on solar latitude λ may be exhibited in spite of our simplified geometry. The initial tube orientation $\hat{\mathbf{x}}$ is the toroidal ($\hat{\boldsymbol{\phi}}$) direction on the Sun, while $\hat{\mathbf{z}}$ is the radial ($\hat{\mathbf{r}}$) direction. By this association the $\hat{\mathbf{z}} \times \hat{\mathbf{x}} = \hat{\mathbf{y}}$ direction corresponds to the $\hat{\mathbf{r}} \times \hat{\boldsymbol{\phi}} = -\hat{\boldsymbol{\theta}}$ direction on the Sun (i.e. northward). The cross product appearing in (8) is therefore

$$\boldsymbol{\omega} \times \hat{\mathbf{y}} \rightarrow -\boldsymbol{\omega} \times \hat{\boldsymbol{\theta}} = -\omega_0 \sin(\lambda)\, \hat{\boldsymbol{\phi}} \rightarrow -\omega_0 \sin(\lambda)\, \hat{\mathbf{x}} \ , \qquad (10)$$

where $\omega_0 = 3\times 10^{-6}$ rad s^{-1} is the mean solar rotation frequency. On making the substitution

$$y_1^{(\mathrm{c})}(s,t) = \sin(\lambda)\, \tilde{y}_1^{(\mathrm{c})}(s,t) \ , \qquad (11)$$

in (8), it is easily found that $\tilde{y}^{(\mathrm{c})}(s,t)$ satisfies a latitude-independent equation

$$\frac{d^2 \tilde{y}_1^{(\mathrm{c})}}{dt^2} + \gamma \frac{d\tilde{y}_1^{(\mathrm{c})}}{dt} - \frac{1}{4\pi\rho_0}\frac{\partial}{\partial s_0}\left(B_0^2 \frac{\partial \tilde{y}_1^{(\mathrm{c})}}{\partial s_0}\right) = -2\omega_0\, v_{x,0} \ . \qquad (12)$$

As the apex of the rising tube ($s = s_{\rm a}$) drains, one expects $v_{x,0} > 0$ for the leading side ($s > s_{\rm a}$) and $v_{x,0} < 0$ for the trailing side ($s < s_{\rm a}$). According to (12), this will drive $\tilde{y}_1^{(\rm c)}(s) < 0$ in the leading portion of the tube. Referring to (11), this is a deflection in the $-\hat{\mathbf{y}}$, or $+\hat{\boldsymbol{\theta}}$, direction in the Northern hemisphere and the opposite direction in the Southern hemisphere. Thus the leading side of the rising tube is deflected equator-ward in each hemisphere, in accordance with Joy's law.

The rise phase ends at $t = t_{\rm e}$ when the tube axis has largely ceased its rise and is in a state of near equilibrium $\mathbf{r}_0(s, t_{\rm e}) = \mathbf{R}_0(s)$. At this time $\mathbf{v}_0 = \gamma = 0$ so that the equation (6) for the perpendicular dynamics becomes an undamped,[1] undriven wave equation

$$\frac{\partial^2 y_1}{\partial t^2} - \frac{1}{4\pi\rho_0}\frac{\partial}{\partial s}\left(B_0^2 \frac{\partial y_1}{\partial s}\right) = 0 \quad . \tag{13}$$

This will be the central equation governing the relaxation phase. Hereafter, we omit the subscript 1 for simplification and set $t = 0$ from the time when relaxation begins (i.e. the clock is set back to zero at the end of the rise phase $t = t_{\rm e}$). The initial condition for the relaxation phase will be given by

$$y(s,0) = Y^{(\rm c)}(s) + Y^{(\rm t)}(s) \quad , \tag{14}$$

where

$$Y^{(\rm c)}(s) = y^{(\rm c)}(s, t_{\rm e}) = \sin(\lambda)\,\tilde{y}^{(\rm c)}(s, t_{\rm e}) \quad , \tag{15}$$

$$Y^{(\rm t)}(s) = y^{(\rm t)}(s, t_{\rm e}) \tag{16}$$

are the perturbations created during the rise phase. The horizontal displacement $Y^{(\rm c)}(s)$ will contribute a non-random component to the tilt angle, corresponding to Joy's law; its proportionality to the sine of solar latitude is explicit in (15). Statistical deviations from Joy's law arise due to the random contribution $Y^{(\rm t)}(s)$; its amplitude will depend on the coupling to convection zone turbulence during the rise of the tube (Longcope and Fisher, 1996).

The coefficients in the wave equation depend on s through the equilibrium tube configuration $\mathbf{R}_0(s)$. If we assume that the length scales of perturbations are smaller than that of $B_0(s)$, we may further simplify (13) to the classic wave equation

$$\frac{\partial^2 y}{\partial t^2} = v_{\rm A}^2(s)\frac{\partial^2 y}{\partial s^2} \quad , \tag{17}$$

where $v_{\rm A} \equiv B/\sqrt{4\pi\rho}$ is the Alfvén speed. Thus the perturbations travel on the equilibrium flux tube as kink modes at the Alfvén speed. In previous treatments (Ryutov and Ryutova, 1976; Spruit, 1981) the wave speed is smaller by $1/\sqrt{2}$ due to the inclusion of enhanced inertia effects which we have neglected here.

In reality, the Alfvén speed $v_{\rm A}(s)$ will vary with s, but the nature of this variation is not very clear. At a depth of 10 Mm below the surface, it is

[1] Without zeroth-order motion the aerodynamic drag is quadratic in $\dot{y}_1$ and therefore absent from our linear treatment.

about 3.2×10^4 cm s^{-1} (taking the magnetic field as 3000 G and density 7×10^{-4} gm cm^{-3}). On the other hand, the Alfvén speed at the bottom of the convection zone, where the density is about 0.2 gm cm^{-3}, is $0.63B$ cm s^{-1}, B being the magnetic field within the flux tube in G. For the two extreme values 100 kG and 20 kG of B, the Alfvén speed at the bottom turns out to be 6.3×10^4 cm s^{-1} and 1.3×10^4 cm s^{-1} respectively. Thus the Alfvén speed at the bottom is of the same order as the Alfvén speed slightly below the surface. Given the various uncertainties in the problem, it is perhaps not a bad approximation to take the Alfvén speed to be a constant. The case of dynamic disconnection, whereby $v_{\mathrm{A}} = 0$ at some point along the tube, is inconsistent with this assumption. This case will be considered in a separate section once the simpler behavior of a uniform Alfvén speed has been explored.

4. Relaxation without dynamic disconnection

To illustrate some basic properties of the relaxation phase we consider a simple solution of Equation (17) with constant Alfvén speed. We have pointed out that it is reasonable to assume a thin flux tube with constant Alfvén speed beneath the photosphere. Above the photosphere, however, both the pressure and mass density drop dramatically. This leads to deconfinement of the magnetic field and to an increase in the Alfvén speed in the solar corona. We may choose to ignore both of these facts and retain a thin flux tube in the corona whose Alfvén speed matches that in the convection zone. This simplifying assumption permits analytical solutions for the relaxation of configurations. A more realistic, but still idealized, approach assumes that the coronal field has no effect on the flux tube below the photosphere. In this case the tube consists of two separate pieces with stress-free boundary conditions at their photospheric surfaces. Once again the evolution may be solved analytically. These two approaches, presented in the two sub-sections below, give similar predictions for the observed bipolar tilt angle. The truth presumably lies somewhere between their extreme assumptions.

4.1. Analytical model with constant Alfvén speed

If the Alfvén speed is assumed constant throughout the flux tube, including the part above the photosphere, we can choose our units suitably to make the Alfvén speed equal to unity such that the wave equation becomes

$$\frac{\partial^2 y}{\partial t^2} = \frac{\partial^2 y}{\partial s^2}. \tag{18}$$

Measuring s from the topmost (coronal) point of the flux tube, the perturbation produced by the Coriolis force can be approximated by the function

$$Y^{(\mathrm{c})}(s) = \theta_{\mathrm{J}} s e^{-s^2}. \tag{19}$$

The constant θ_{J} is the tilt angle according to Joy's law.

To understand the effect of perturbations produced by turbulence in a narrower region of the flux tube around $s = 0$, we superpose on this a function

$$Y^{(\mathrm{t})}(s) = \theta_{\mathrm{J}} cse^{-\beta s^4}, \tag{20}$$

which is localized to a narrow region provided β is sufficiently large. According to (14), the initial configuration of the flux tube is

$$y(s,0) = \theta_{\mathrm{J}}[se^{-s^2} + cse^{-\beta s^4}], \tag{21}$$

while the initial velocity is taken as zero, i.e.

$$\frac{\partial y}{\partial t} = 0. \tag{22}$$

Figure 3 shows three versions of initial condition (21) with $\beta = 1000$ and $c = 0, \pm 2$.

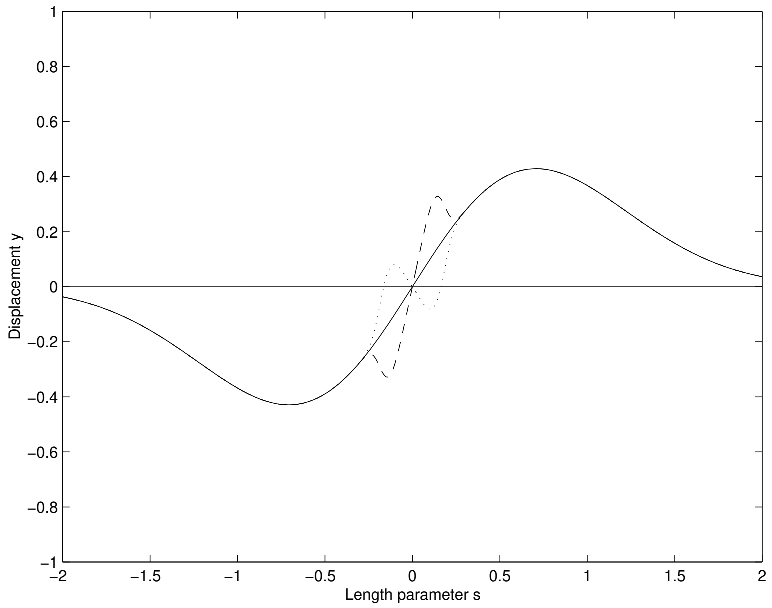

Figure 3. Top views of several possible configurations of the flux tube after the rise phase. The middle point ($s = 0$) corresponds to the top of the flux tube, The solid curve shows a tube not disturbed by turbulence ($c = 0$). The dashed and dotted curves are tubes with different turbulent distortions ($c = \pm 2$).

In our example, the Coriolis displacement decreases rapidly to zero for s slightly larger than 2. Since the Coriolis force acts on all rising portions of the tube, the region $-2 \leq s \leq 2$ must correspond to regions within the convection zone. This means that our initial conditions have a unit length is about 1.2×10^{10} cm. With the Alfvén speed set to unity, the unit of time will be 9.2×10^5 s (i.e. 11 days) or 1.9×10^5s (i.e. 2.2 days) respectively for Alfvén speeds of 1.3×10^4 cm s^{-1} or 6.3×10^4 cm s^{-1} (corresponding to basal magnetic fields of 20 kG and 100 kG respectively). It can be seen from Figure 3 that the flux tube has the correct tilt (i.e. similar to Joy's law) at a value of s about 0.3, which corresponds to 36 Mm. Assuming that a part of the flux tube is above the photosphere, our model is then restricting the effect of turbulence to the top 30 Mm or so of the convection zone.

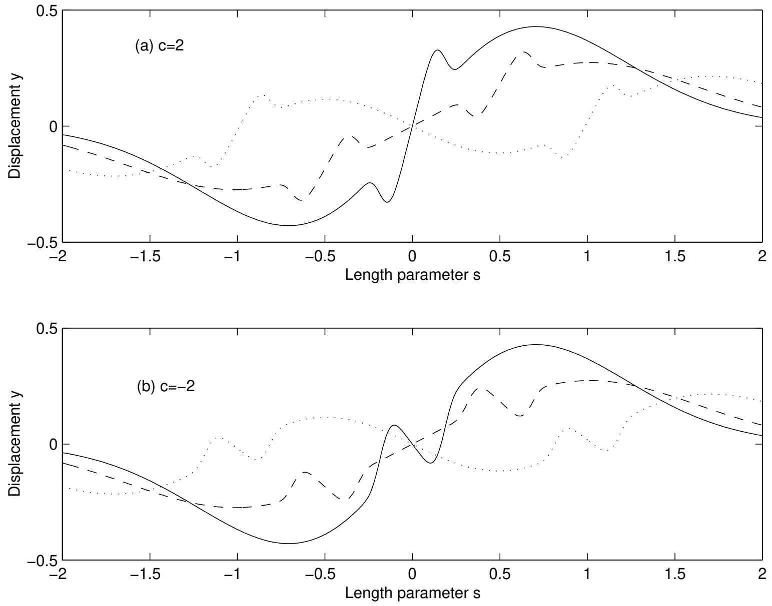

Figure 4. The configurations of the flux tube at times 0, 0.5 and 1 for the cases (a) $c = 2$ and (b) $c = -2$.

The solution to the wave equation (18) with the initial conditions (21)–(22) is

$$\begin{aligned} y(s,t) &= \frac{1}{2}\theta_{\rm J}[(s+t)e^{-(s+t)^2} + (s-t)e^{-(s-t)^2}] \\ &+ \frac{1}{2}\theta_{\rm J}c[(s+t)e^{-\beta(s+t)^4} + (s-t)e^{-\beta(s-t)^4}] \quad . \end{aligned} \tag{23}$$

Figures 4a and 4b show the evolution of two of the initial configurations from Figure 3. In this simple model, the tilt angle at the top of the flux tube is

$$\theta = \left.\frac{\partial y}{\partial s}\right|_{s=0} \quad . \tag{24}$$

Substituting for y from (23), gives a time-evolving tilt angle

$$\theta(t) = \theta_{\rm J}[e^{-t^2}(1-2t^2) + ce^{-\beta t^4}(1-4\beta t^4)] \quad . \tag{25}$$

This function is plotted in Figure 5 for the values $c = 0, \pm 2$, for which the initial configurations have been shown in Figure 3.

It is evident from Figure 5a that the tilt angle relaxes to $\theta_{\rm J}$ given by Joy's law in about 0.4 time units. In order for this relaxation time to correspond to 4.37 days, the value observed by Howard, the Alfvén speed must be 1.3×10^4 cm s^{-1}. This is slightly smaller than 3.2×10^4 cm s^{-1}, the estimated Alfvén speed at a depth of 10 Mm.

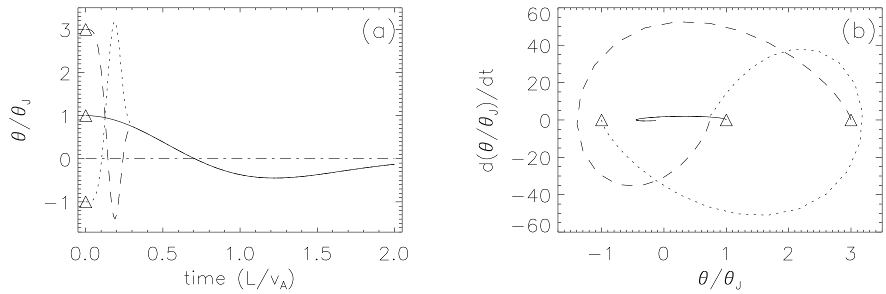

Figure 5. The evolution of tilt angle $\theta(t)/\theta_J$. (a) Plotted versus t for the cases $c = 0$ (solid line), $c = 2$ (dashed line) and $c = -2$ (dotted line). (b) The same cases as $\dot{\theta}$ vs. θ. The initial positions are marked with triangles.

We show in a more sophisticated calculation in Section 5 that agreement with the observed relaxation time requires propagation speeds somewhat lower than the Alfvén speed estimated at 10 Mm. One possibility is that the Alfvén speed in deeper layers is somewhat lower and the effective Alfvén speed of our simple constant-speed models should be taken from somewhat deeper layers. If we assume that the magnetic field inside the flux tube continues to have a value around 3000 G for some depth, then the density has to be 4.2×10^{-3} gm cm^{-3} to make the Alfvén speed equal to 1.3×10^4 cm s^{-1}. According to the model of Spruit (1974), this happens at a depth of 24 Mm, which is not unreasonable. We hereafter use $v_{\rm A} = 1.3 \times 10^4$ cm s^{-1} as a value for the Alfvén speed in our uniform flux tube.

We thus find that our simple model gives the rough order-of-magnitude of the time scale for orientational relaxation toward Joy's law. This model also predicts that tilts will eventually relax to $\theta = 0$ (i.e. parallel to the equator) after about 1 unit of time. If 0.4 is fixed to 4.37 days, then relaxation to $\theta = 0$ should occur after 10 days. Such a relaxation to zero tilt is inevitable in the absence of dynamic disconnection, owing to the tension force from toroidal anchor points. We return below to consider possible evidence for this second-stage relaxation in the observational data.

To match the analysis of Howard (1996) we plot $\dot{\theta}(t)$ vs $\theta(t)$ for our simple model. Differentiating (25) with respect to t gives

$$\dot{\theta}(t) = -\theta_{\rm J}[e^{-t^2}(6t - 4t^3) + ce^{-\beta t^4}(20\beta t^3 - 16\beta^2 t^7)]. \qquad (26)$$

Each initial condition, specified by c, will trace a curve in the $\dot{\theta}$ versus θ plane as it evolves. Figure 5b shows such trajectories for $c = \pm 2$. The Mount Wilson data set consists of snapshots from many such curves, each with different initial conditions. In section 5, we derive general properties of this.

4.2. Model with stress-free photospheric boundary condition

A flux tube that has emerged through the solar surface has subsurface parts below the two photospheric poles of the active region. We can model such a flux tube as two separate pieces communicating with one another only weakly if at all. We shall follow the relaxation of the leading-side piece and mirror its dynamics to obtain the following-side relaxation. We measure s downward along the leading-side flux tube starting from its photospheric intersection, $s = 0$. Since this photospheric intersection is free to move horizontally, it can support no horizontal stress; the tube must be vertical there. This imposes the boundary condition

$$\left.\frac{\partial y}{\partial s}\right|_{s=0} = 0 \quad , \tag{27}$$

on first-order displacements. We shall place no boundary condition on the downward side because the flux tube joins the toroidal flux at the base of the convection zone.

The transverse displacement at the solar surface, $y(0,t)$, defines the observed properties of the bipole, such as its tilt angle. Assuming that the following pole has exactly the opposite distortion as the leading pole, and that they are separated by the toroidal distance Δx, the observed tilt angle of the bipole is

$$\theta(t) = \mp \sin^{-1}[2y(0,t)/\Delta x] \simeq -2\Delta x^{-1}\,\mathrm{sgn}(\lambda)\,y(0,t) \quad , \tag{28}$$

where we have assumed the displacement to be small relative to the pole separation Δx. We follow the convention used by Howard in which $\theta > 0$ corresponds to a bipole with an equator-ward leading spot, in accordance with Joy's law. In the second expression of (24), the upper sign is for bipoles in the Northern hemisphere ($\lambda > 0$); in the third expression, we use the signum function to make this distinction.

The horizontal displacement $y(s,t)$ evolves from its initial condition according to the wave equation (17). If the Alfvén speed is uniform along the flux tube underneath the photospheric surface, the full solution can be written as a sum of upward and downward propagating waves. Assuming no initial velocity, $\partial y/\partial t = 0$, the upward and downward waves are given by half the initial conditions. Defining the $s < 0$ portions of the initial conditions by reflecting the $s > 0$ portions allows the full solution to be written

$$y(s,t) = \frac{1}{2}[Y^{(\mathrm{c})}(s-v_{\mathrm{A}}t)+Y^{(\mathrm{t})}(s-v_{\mathrm{A}}t)] + \frac{1}{2}[Y^{(\mathrm{c})}(s+v_{\mathrm{A}}t)+Y^{(\mathrm{t})}(s+v_{\mathrm{A}}t)] \ .$$

By making each function even in its arguments, we have guaranteed that this expression automatically satisfies (27) as well as the initial conditions on $y(s,t)$ and $\partial y/\partial t$. Figure 6 shows the relaxation of a vertical flux tube.

While Figure 4a and Figure 6, are views from different perspectives, they each depict the relaxation of perturbations due to the Coriolis force and turbulence, which deflect the flux tube from the plane of rise. The tilt angle and the tilt angle change are simply given by

$$\theta(t) = -2\,\mathrm{sgn}\lambda\,\Delta x^{-1}[\,Y^{(\mathrm{c})}(v_{\mathrm{A}}t) + Y^{(\mathrm{t})}(v_{\mathrm{A}}t)\,] \ , \tag{29}$$

$$\dot{\theta}(t) = -2\,\mathrm{sgn}\lambda\,v_{\mathrm{A}}\Delta x^{-1}[\,\dot{Y}^{(\mathrm{c})}(v_{\mathrm{A}}t) + \dot{Y}^{(\mathrm{t})}(v_{\mathrm{A}}t)\,] \ . \tag{30}$$

The bottom panel of Figure 6 depicts the evolution of θ with time, analogous to 4b.

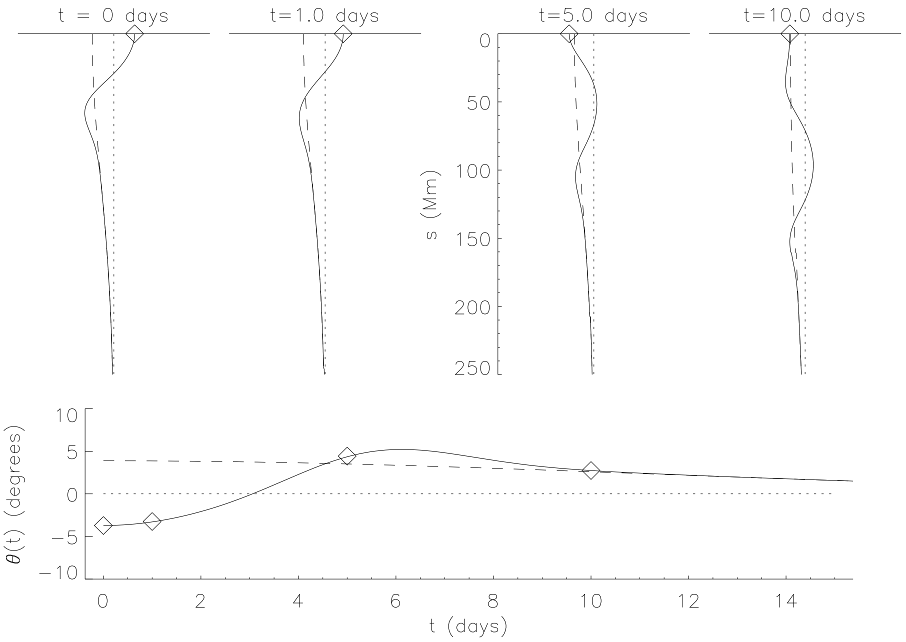

Figure 6. An example of a distorted flux tube $y(s,t)$ evolving. The initial state ($t=0$) is composed of a Coriolis contribution $Y^{(\mathrm{c})}$ (shown dashed) and a random distortion from convection zone turbulence $Y^{(\mathrm{t})}$. The distortion relaxes according to the wave equation with an open boundary condition at the solar surface ($s=0$). The observed tilt is given, in degrees, by the horizontal displacement at $s=0$, graphed along the bottom. The dashed curve shows the evolution of the tilt angle for distortion due to the Coriolis force alone.

5. Application to data statistics

The analytical results presented above can be used to explain statistical trends in the data set of Howard. We apply the model developed in Section 4.2 to a large number of bipolar spot groups with different ages and different turbulent perturbation. This leads to a synthetic data set of $\dot{\theta}_i$ versus θ_i, from which statistical trends are identified, and compared to those in the Mount Wilson sunspot survey.

5.1. The data set

The data set consists of N observations θ_i and $\dot{\theta}_i$. Observation i is a sunspot group at latitude λ_i whose age (i.e. time since its moment of emergence) is t_i. According to the theory of Section 4.2, we have

$$\theta_i \;=\; -2\,\mathrm{sgn}\lambda_i\,\Delta x^{-1}[\,Y_i^{(\mathrm{c})}(v_{\mathrm{A}}t_i) \;+\; Y_i^{(\mathrm{t})}(v_{\mathrm{A}}t_i)\,]\;\;, \tag{31}$$

$$\dot{\theta}_i \;=\; -2\,\mathrm{sgn}\lambda_i\,v_{\mathrm{A}}\Delta x^{-1}[\,\dot{Y}_i^{(\mathrm{c})}(v_{\mathrm{A}}t_i) \;+\; \dot{Y}_i^{(\mathrm{t})}(v_{\mathrm{A}}t_i)\,]\;\;, \tag{32}$$

where $Y_i^{(\mathrm{c})}$ depends on the latitude λ_i and $Y_i^{(\mathrm{t})}$ is a single realization of a random function.

We shall assume, for simplicity, that all N observations are statistically independent of one another so that $Y_i^{(\mathrm{t})}$ and $Y_j^{(\mathrm{t})}$ are uncorrelated random variables provided $i \neq j$. The statistics of $Y_i^{(\mathrm{t})}$ follow from the statistics of the turbulent velocity v_y^{e} which generated it. An ensemble average of (9) shows that $\langle Y^{(\mathrm{t})} \rangle = 0$, since the turbulent velocity must have zero mean, $\langle v_y^{\mathrm{e}} \rangle = 0$. Estimating the average tilt angle from the large data set gives

$$\langle \theta \rangle = \frac{1}{N} \sum_i \theta_i \;\simeq\; -\frac{2}{\Delta x\, N} \sum_i \mathrm{sgn}\lambda_i \, Y_i^{(\mathrm{c})}(v_{\mathrm{A}} t_i) \quad , \tag{33}$$

since the sum of the random values $Y_i^{(\mathrm{t})}$ approximately vanishes. Equation (15) shows that $Y^{(\mathrm{c})}(s)$ is proportional to $\sin(\lambda_i)$, so terms will be the same sign in each hemisphere.

If the entire data set were drawn from latitude λ then the average tilt angle would be a measurement of Joy's law

$$\frac{1}{N} \sum_i \theta_i \;\equiv\; \theta_{\mathrm{J}}(\lambda) \;\simeq\; -\frac{2\,|\sin(\lambda)|}{\Delta x\, N} \sum_i \tilde{y}_i^{(\mathrm{c})}(v_{\mathrm{A}} t_i, t_{\mathrm{e}}) \quad , \tag{34}$$

where (15) has been used. As previously discussed, we expect $\tilde{y}^{(\mathrm{c})}(s,t) < 0$ on the leading side of the loop ($s > 0$) so that Joy's law angle is positive. While θ_{J} is proportional to $|\sin(\lambda)|$, the essence of Joy's law, the measured value will also depend on the ages of the sunspot groups in the data set. Furthermore, the latitude-independent distortion $\tilde{y}_i^{(\mathrm{c})}$ depends on properties of the rising flux tube such as its total flux Φ_i.

5.2. The tilt angle change

The observation which motivated this work is a trend in $\dot{\theta}_i$ versus θ_i evident in a large data set. Howard (1996) binned the data in θ_i and fit a line to the average $\dot{\theta}_i$ in each bin (Figure 4 in Howard 1996). He found that the fit intersected $\dot{\theta} = 0$ at an angle comparable to $\langle \theta \rangle$. Except for sampling effects and a 180° ambiguity, not present in a theoretical model, the same can be found from a linear-least-squares fit to the complete data set. The x-intercept of such a linear-least-squares fit is (see, for example, Press *et al.*, 1986, Chapter 14)

$$\theta_x \;=\; \frac{\langle \theta\dot{\theta} \rangle \langle \theta \rangle - \langle \theta^2 \rangle \langle \dot{\theta} \rangle}{\langle \theta\dot{\theta} \rangle - \langle \theta \rangle \langle \dot{\theta} \rangle} \tag{35}$$

where each of the averages are over the data set $i = 1$ to N. By analogy to (33), we find

$$\langle \theta^2 \rangle = \frac{1}{N} \sum_i \theta_i^2 \;\simeq\; \frac{4}{\Delta x^2\, N} \sum_i \{\, [Y_i^{(\mathrm{c})}(v_{\mathrm{A}} t_i)]^2 + [Y_i^{(\mathrm{t})}(v_{\mathrm{A}} t_i)]^2 \,\} \quad . \tag{36}$$

Since the statistical fluctuations about Joy's law are observed to be much greater than its mean (Fisher, Fan, and Howard, 1995), we expect $|Y^{(\mathrm{t})}| \gg |Y^{(\mathrm{c})}|$ and can approximate

$$\langle \theta^2 \rangle \;\simeq\; \frac{4}{\Delta x^2\, N} \sum_i [Y_i^{(\mathrm{t})}(v_{\mathrm{A}} t_i)]^2 \quad . \tag{37}$$

The averages with time derivatives can be similarly approximated

$$\langle\dot{\theta}\rangle \simeq -\frac{2\,v_{\rm A}}{\Delta x\,N}\sum_i {\rm sgn}\lambda_i\,\dot{Y}_i^{\rm (c)}(v_{\rm A}t_i) \quad , \tag{38}$$

$$\langle\theta\dot{\theta}\rangle \simeq \frac{4\,v_{\rm A}}{\Delta x^2\,N}\sum_i Y_i^{\rm (t)}(v_{\rm A}t_i)\dot{Y}_i^{\rm (t)}(v_{\rm A}t_i) \quad . \tag{39}$$

The numerator of equation (35) for the intercept can be written

$$\langle\theta\dot{\theta}\rangle\langle\theta\rangle - \langle\theta^2\rangle\langle\dot{\theta}\rangle = \langle\theta^2\rangle\langle\theta\rangle\left[\frac{\langle\theta\dot{\theta}\rangle}{\langle\theta^2\rangle} - \frac{\langle\dot{\theta}\rangle}{\langle\theta\rangle}\right] \quad . \tag{40}$$

Referring to expressions for each average, we can see that the factor in square brackets is a difference in relaxation rates. The first term involves only the turbulent-driven distortions, while the second involves only the Coriolis driven distortions. Only if the Coriolis and turbulent contributions relaxed at identical rates would we expect a cancellation yielding $\theta_x = 0$. It is our contention that the turbulence-driven contribution relaxes more rapidly leading to an intercept $\theta_x \sim \langle\theta\rangle$.

The variance in tilt angle given by (37) reflects the mean square amplitude of turbulent-driven fluctuations at a sampling of depths $s_i = v_{\rm A}t_i$. Let us define a function $F(\delta s)$ to be that same amplitude sampled at distances δs below the original points

$$F(\delta s) \equiv \frac{1}{N}\sum_i [Y_i^{\rm (t)}(v_{\rm A}t_i + \delta s)]^2 \quad . \tag{41}$$

We expect the fluctuation amplitude $F(\delta s)$ to decrease as the samples move deeper into the convection zone where turbulence is weaker, and the tension force is greater. Based on the discussions in Section 2, we expect turbulent fluctuations to be absent at depths significantly below $z = 30$ Mm, the turbulent distortion depth. From (37) and (39), we get

$$\frac{\langle\theta\dot{\theta}\rangle}{\langle\theta^2\rangle} = \frac{v_{\rm A}F'(0)}{2F(0)} \quad . \tag{42}$$

This decay rate is $v_{\rm A}$ divided by the twice the characteristic scale of the turbulence amplitude. To determine the relative importance of the two terms in (40), this length must be compared with the length scale of the Coriolis-induced distortion; we expect this to be ~ 200 Mm, comparable to the size of the Ω-loop. According to the discussion in Section 2, we expect the turbulent perturbation to decrease on a length scale of 30 Mm, or less. This discrepancy permits us to neglect the second term in (40), i.e. $\langle\theta\dot{\theta}\rangle\langle\theta\rangle \gg \langle\theta^2\rangle\langle\dot{\theta}\rangle$. Using this in the equation (35) for the intercept θ_x, we get

$$\theta_x \simeq \frac{\langle\theta\dot{\theta}\rangle\langle\theta\rangle}{\langle\theta\dot{\theta}\rangle - \langle\theta\rangle\langle\dot{\theta}\rangle} \simeq \langle\theta\rangle \quad , \tag{43}$$

where the final expression follows from $\langle\theta\dot{\theta}\rangle \gg \langle\theta\rangle\langle\dot{\theta}\rangle$, which in turn follows from $\langle\theta^2\rangle \gg \langle\theta\rangle^2$ as established above. Thus we find the intercept $\theta_x \simeq \theta_{\rm J}$ in agreement with the analysis of Howard (1996).

5.3. The relaxation rate

The slope of the linear fit

$$\nu \; = \; \frac{\langle\theta\dot{\theta}\rangle - \langle\theta\rangle\langle\dot{\theta}\rangle}{\langle\theta^2\rangle - \langle\theta\rangle^2} \quad , \tag{44}$$

is interpreted as the relaxation rate for individual sunspot pairs. Using the approximations from above, this becomes

$$\nu \; \simeq \; \frac{\langle\theta\dot{\theta}\rangle}{\langle\theta^2\rangle} \; = \; \frac{1}{2}v_{\mathrm{A}}\frac{F'(0)}{F(0)} \quad , \tag{45}$$

which will be negative since F is a decreasing function of its argument. Setting this to the observed value of $\nu = -0.229\,\mathrm{day}^{-1}$ yields

$$-\frac{F'(0)}{F(0)} \; = \; v_{\mathrm{A}}^{-1}\,5.3\times10^{-6}\,\mathrm{sec}^{-1} \quad . \tag{46}$$

Adopting $v_{\mathrm{A}} = 1.3\times10^4$ cm s^{-1} characteristic of shallow depths, we get a characteristic length $\ell = F(0)/F'(0) = 24$ Mm. This is comparable to the turbulent distortion depth thereby corroborating the assumption made in the previous section.

5.4. A synthetic data set

We illustrate the foregoing analysis with a synthetic data set θ_i and $\dot{\theta}_i$, generated using Monte Carlo techniques. The synthetic data, shown in Figure 7, follow from simple models for the functions $Y^{(\mathrm{c})}(s)$ and $Y^{(\mathrm{t})}(s)$, described in the Appendix. The plot includes sunspot groups from latitudes $-30^\circ \le \lambda_i \le 30^\circ$ and ages t_i exponentially distributed with a mean of 3 days. The data contains the same linear trend and non-zero intercept observed by Howard (1996), and predicted by the above calculation. The qualitative agreement between our Figure 7 and Figure 3 of Howard (1996), reproduced as our Figure 1, shows the basic soundness of our model.

As noted in Section 4, the flux tubes without dynamic disconnection will inevtiably align East-West. Our analytic solution showed that by 10 days after emergence the turbulent perturbations have propagated away, and the relaxation is toward $\theta = 0$. If the model is correct, and dynamic disconnection is absent, the intercept of the $\dot{\theta}_i$ vs. θ_i plot would be $\theta = 0$, as anticipated by Howard. A subset of the older bipoles from within the existing data should show this behavior. Figure 8 shows the results of the same Monte Carlo simultion from Figure 7, except that only bipoles with $t_i \ge 7$ days have been plotted. The least-squares fit shows an intercept much closer to $\theta = 0$, and a relaxation rate of $\nu = -0.097\,\mathrm{day}^{-1}$. These same data points are present in Figure 7, but their trend is obscured by the overwhelming majority of younger bipoles. We show below that this result is not present in a model with dynamic disconnection. The fact that the eventual relaxation to $\theta = 0$ cannot easily be noted in Figure 7 should have important implications for observational data of real spot groups. To determine observationally whether

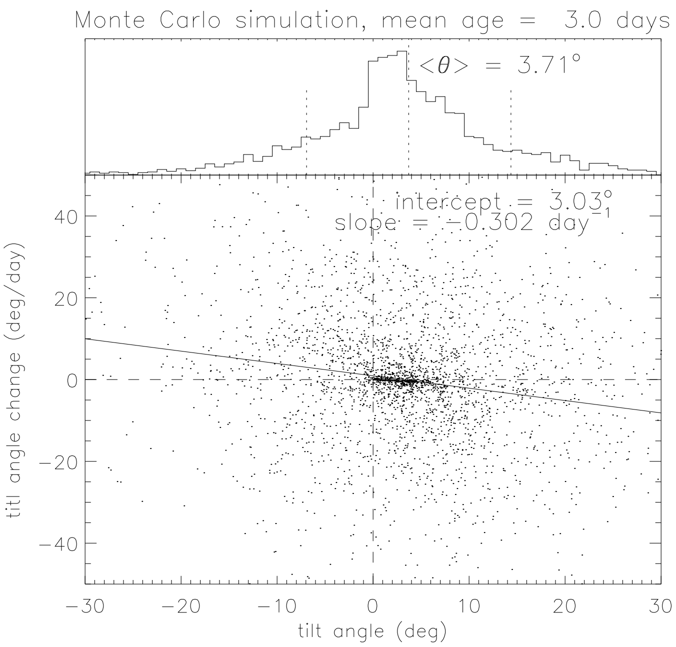

Figure 7. A synthetic data set of tilt angles and their changes. The data points are generated from a sampling of latitudes and ages (with an average age of 3 days). A least-squares fit shows a slope and intercept comparable to those found by Howard. A histogram of the tilt-angle data is shown across the top, showing that the mean and scatter are similar to those in the Wilson sunspot data.

eventual toroidal relaxation takes place, one should separate out the older spot groups and try to produce a plot like our theoretical Figure 8. Just because nobody has so far reported the tendency towards eventual toroidal relaxation of spot groups, we cannot conclude that such a tendency does not exist. We believe that nobody has yet analyzed the observational data in an appropriate way to look for this effect. We urge the reader to look at Figure 6 of Howard (1996), where growing and decaying spot groups are plotted separately. It is clear that the decaying spot groups relax toward a value of θ smaller than θ_J with a slower relaxation rate.

6. The effect of dynamic disconnection

The analysis of the two previous sections assumed the Alfveén speed v_{A} to be uniform along the flux tube under the solar surface. Because of this assumption, all perturbations propagate without dispersion along the tube. The amount of perturbation in the topmost part of the tube decreases with time, as a result of the perturbation propagating downward indefinitely, ultimately turning the bipole to perfectly toroidal alignment. If, however, the downward propagation is blocked at some depth, then the evolution of the flux tube can be completely different. It has been proposed that an equilibrium flux tube becomes dynamically disconnected at some point $s = s_{\mathrm{dd}}$ (Fan, Fisher, and

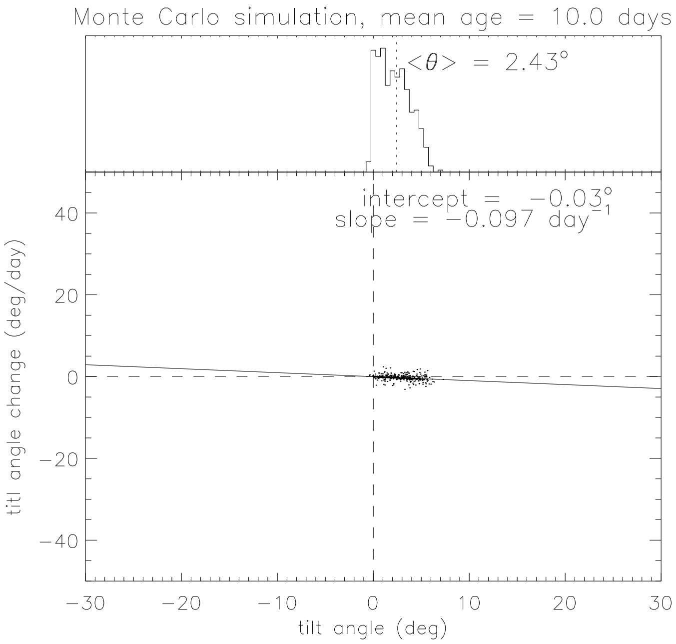

Figure 8. A subset of the synthetic data set from Figure 7 including only bipoles with $t_i \geq 7$ days. The lifetimes are still expontential distributed with a characteristic life of 3 days, therefore the mean age is 10 days.

McClymont, 1994) and will not be driven toward toroidal alignment. Here we investigate the effect of dynamic disconnection on the tilt relaxation, and seek evidence for it in the data set.

We shall use the stress-free photospheric boundary condition, as in Section 4.2, and shall focus our attention on the leading part of the flux tube. Once more, s increases downward starting from the photospheric intersection at $s = 0$. The Alfvén velocity is not constant, but decreases to zero at the depth of dynamic disconnection $s_{\rm dd}$ where the magnetic field strength of the equilibrium tube vanishes, $B(s_{\rm dd}) = 0$. In this case we must solve the non-uniform wave equation (13). Introducing the mass variable m and associated phase velocity $w_{\rm A}$

$$m(s_0) \;\equiv\; \int_0^{s_0} \rho(s)\,ds \quad , \quad w_{\rm A}(s_0) \;\equiv\; \rho v_{\rm A} \;=\; \sqrt{\frac{B^2\rho}{4\pi}} \quad , \tag{47}$$

the wave equation takes the form

$$\frac{\partial^2 y}{\partial t^2} \;-\; \frac{\partial}{\partial m}\left[w_{\rm A}^2(m)\,\frac{\partial y}{\partial m}\right] \;=\; 0 \quad . \tag{48}$$

A flux tube which is dynamically disconnected at $s = s_{\rm dd}$ will have $w_{\rm A}(m_{\rm dd}) = 0$, where $m_{\rm dd} = m(s_{\rm dd})$. As a simple model for this behavior, we will adopt the functional description

$$w_{\rm A}(m) \;=\; w_{\rm A}(0)\,(1 - m/m_{\rm dd})^{1/2} \quad , \tag{49}$$

so that the magnetic field vanishes as $(s_{\rm dd} - s)^{1/2}$. With this weak singularity, the total mass within the disconnected tube is finite, even as the cross sectional diameter diverges. The resulting wave equation (48) is analogous to that for perturbations on a freely hanging string; the free end of the string corresponds to the point of dynamic disconnection.

A few steps of strightforward mathematics show that the equation (48) with $w_{\rm A}(m)$ given by (49) is satisfied by

$$y(m,t) \;=\; \cos(\omega t)\, J_0\left(\frac{2m_{\rm dd}}{w_{\rm A}(0)}\omega\sqrt{1-m/m_{\rm dd}}\right) \quad , \tag{50}$$

where J_0 is the Bessel function of order zero. The stress-free boundary condition at the surface is

$$\left.\frac{\partial y}{\partial m}\right|_{m=0} \;=\; 0, \tag{51}$$

which follows from (27). Substituting our solution into this boundary condition, we obtain

$$J_1\left(\frac{2m_{\rm dd}}{w_{\rm A}(0)}\omega\right) = 0. \tag{52}$$

This shows that ω must have a discrete spectrum. If $j_{1,n}$ is the $n^{\rm th}$ root of $J_1(x) = 0$, then the discrete values of ω are given by

$$\omega_n = j_{1,n}\omega_0, \tag{53}$$

where ω_0 is the fiducial frequency

$$\omega_0 \;\equiv\; \frac{w_{\rm A}(0)}{2m_{\rm dd}} \;=\; \frac{1}{2}v_{\rm A}(0)\left[\int_0^{s_{\rm dd}}\rho(s)/\rho(0)\,ds\right]^{-1} \quad . \tag{54}$$

For a constant density atmosphere this is $\omega_0 = v_{\rm A}(0)/2s_{\rm dd}$, while for an atmosphere with increasing density the frequency is smaller. The general solution to the wave equation is

$$y(m,t) \;=\; \bar{y} \;+\; \sum_{n=1}^{\infty} A_n\, \cos(j_{1,n}\omega_0 t)\, J_0(j_{1,n}\sqrt{1-m/m_{\rm dd}}) \quad , \tag{55}$$

where A_n are coefficients found from the initial condition. The $n = 0$ term, representing the mass-averaged displacement $\bar{y}$, is a constant of the motion and has been separated from the sum. The displacement at the point of disconnection $m = m_{\rm dd}$ oscillates over time exactly as the free end of a string does.

As before, the observed tilt angle is found from the transverse displacement at the surface $m = 0$:

$$\theta(t) \;=\; -\,2\Delta x^{-1}{\rm sgn}(\lambda)\left[\bar{y} \;+\; \sum_n A_n J_0(j_{1,n})\,\cos(j_{1,n}\omega_0 t)\right] \quad . \tag{56}$$

This is the analog of Equation (29) for a dynamically disconnected flux tube. The initial condition functions, $Y^{\rm (t)}$ and $Y^{\rm (c)}$, determine the coefficients

$$A_n = A_n^{\rm (c)} + A_n^{\rm (t)} \quad ,$$

on which the evolution of θ depends. This further complicates the relationship between initial condition and observed data. Two limiting cases help to illustrate the range of possible behaviors.

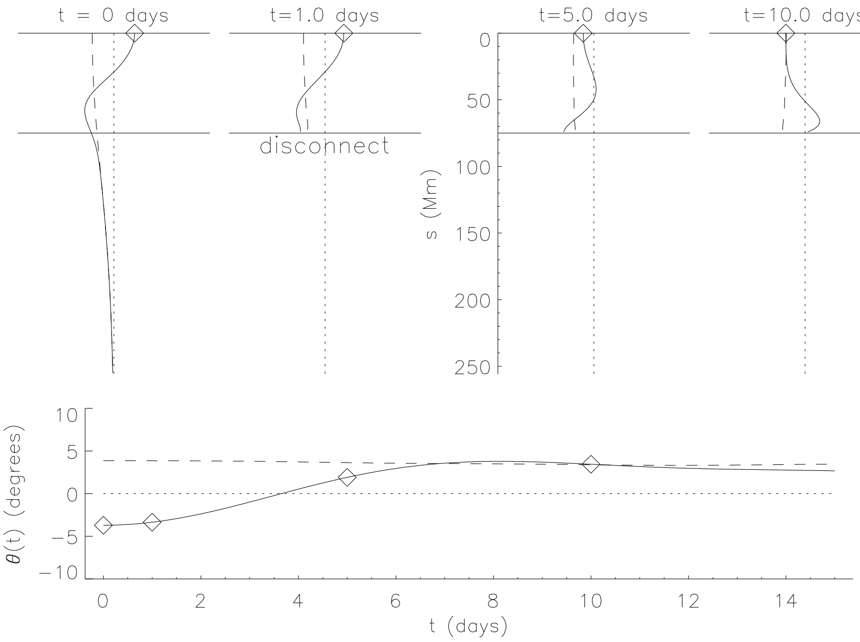

Figure 9. The relaxation of horizontal distortions $y(s,t)$ in a tube which is dynamically disconnected at $s_{\rm dd} = 75$ Mm (shown by a solid horizontal line). The initial condition is identical to that in Figure 6. Note that the Coriolis contribution (dashed line) is fairly straight above 75 Mm, and thus does not disappear over time.

If the spectrum is dominated by a single mode A_k, then the tilt angle $\theta(t)$ will oscillate with period $2\pi/\omega_k$. Such a perturbation excites a standing wave between the solar surface and the disconnection point. Points in a plot of $\dot{\theta}$ versus θ would form an ellipse centered at $|\theta| \simeq -2\bar{y}/\Delta x$.

At the other extreme, the anharmonic oscillations of a broad, flat spectrum will tend to average away over time $t \gg 1/\omega_0$ due to phase mixing. In this case, the tilt angle will approach the asymptotic value $|\theta| \simeq -2\bar{y}/\Delta x$. This demonstrates the expected result that a disconnected flux tube need not align itself in the toroidal direction even after long times. Instead, the direction of asymptotic alignment will depend on the mass-averaged displacement of the tube segment above the point of disconnection.

The actual perturbation spectrum depends on the functions $Y^{(\rm c)}$ and $Y^{(\rm t)}$ between $s = 0$ and the disconnection point $s_{\rm dd}$. If the disconnection point is deep, it will be hard to detect the effects of disconnection from spot-group data. In this case, the fiducial frequency will be low, reflecting the long travel time to the disconnection point. Furthermore, the perturbation $Y^{(\rm t)}(m)$ will be peaked about $m = 0$ resulting in a broad spectrum A_n. According to above arguments, this will result in asymptotic relaxation to a non-zero angle, but only after very long times $\gg 1/\omega_0$. Immediately after emergence, the turbulent perturbations will propagate away from the surface in a manner similar to the uniform Alfvén speed case. Thus we expect to find no evidence in the data for deep dynamic disconnection.

If dynamic disconnection occurs close to the solar surface, as some investigations suggest (Lundquist and Fisher, 2001) , it will be evident in the $\dot{\theta}$ versus θ plot. The perturbations $Y^{(\mathrm{t})}(s)$ and $Y^{(\mathrm{c})}(s)$ will have very little structure over the short interval $0 < s < s_{\mathrm{dd}}$, so the spectrum will be dominated by the $n = 1$ term. Consequently, the tilt angle will oscillate with a period set by the short travel time to the shallow disconnection point. The distribution of $\dot{\theta}_i$ versus θ_i observed by Howard (1996) is significantly different from the predicted ellipse. Thus it is unlikely that dynamic disconnection occurs at very shallow points. Figure 10 presents results of a Monte Carlo simulation done similarly to that shown in Figure 7, but with dynamic disconnection at $s_{\mathrm{dd}} = 75$ Mm below the surface. Even when dynamic disconnection is assumed at this considerable depth, the resulting theoretical data look very different from the observational data presented in Figure 1.

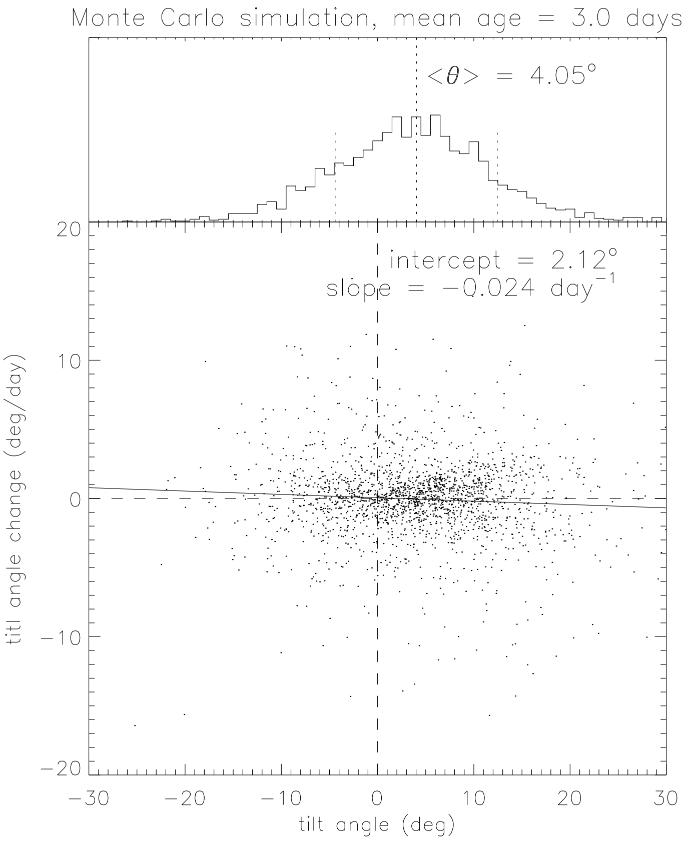

Figure 10. A Monte Carlo simulation with dynamically disconnected flux tubes. The simulation is done exactly as in Figure 7, but with tubes disconnected at $s_{\mathrm{dd}} = 75$ Mm.

The main purpose of invoking dynamic disconnection was to stop the flux tube from relaxing to zero tilt. It is evident ftom the foregoing analysis that it has another profound effect. It prevents the short-wavelength perturbations, produced by turbulence, from propagating away down the flux tube. These perturbations remain confined within the disconnected part of the flux tube, and if the point of disconnection is shallow, then the resulting time evolution is very different from the orientational relaxation in the observational data. We can thus conclusively rule out a dynamic disconnection at a shallow depth soon after the emergence of the active region. In simple terms, there is no way to exhibit a 4.37 day dynamic time scale if the dynamic disconnection layer is significantly shallower than a 4.37 day Alfvén transit. This cannot rule out the possibility that dynamic disconnection takes place at a shallow depth during the decay phase of the active region after the short-wavelength perturbations produced by turbulence have propagated away. This effect would become more evident, however, as an older sub-population of the data were extracted, as in Figure 8.

7. Conclusion

This theoretical investigation was motivated by the observation of Howard (1996) that bipolar active regions initially emerging with tilts inconsistent with Joy's law relax towards the Joy's law tilt angle. Since this orientational relaxation towards Joy's law could not result from the Coriolis force, the observation calls into question the whole scenario that Joy's law is due to the action of the Coriolis force (D'Silva and Choudhuri, 1993). We have shown in this paper, however, that the observations of orientational relaxation are completely consistent with the current theoretical scenario of flux emergence, in which departures from Joy's law are due to distortions created by turbulence (Longcope and Fisher, 1996). These distortions will be confined in the topmost region of the flux tube and therefore have wavelengths short compared to the wavelength of deformation caused by the Coriolis force. We have demonstrated that this discrepancy in length scale means that the turbulent distortions propagate away faster, leaving the deformation due to the Coriolis force. The tilt angle observed therefore appears to relax toward the mean angle, as predicted by Joy's law.

Unless dynamic disconnection takes places, all bipoles will eventually relax to a tilt angle of zero. We have generated synthetic theoretical data by Monte Carlo techniques, both without dynamic disconnection and with it. On comparing with observational data, we can rule out dynamic disconnection at a shallow depth. Apart from stopping the toroidal flux tube alignment, dynamic disconnection also stops the short-wavelength turbulent perturbations from propagating away downward. Hence, dynamic disconnection at a shallow depth would not allow a fast relaxation to Joy's law tilt θ_{J}, as seen in the observational data. We thus not only show that the orientational relaxation of bipolar active regions is consistent with the current scenario of flux emergence, we also argue that the observational data of orientational relaxation can be used as a probe to explore the structure of magnetic field below sunspots—an idea which, to the best of our knowledge, has never been suggested before this work. We have already drawn one firm conclusion. Dynamic disconnection at a shallow depth in the early phase is completely ruled out.

According to our model it is possible to use sunspot data, such as the Mount Wilson digitized sunspot survey, to confirm the eventual toroidal alignment of bipoles. The first step is to supplement the exsiting data with the age of each sunspot group, or a lower bound based on the group's appearance on the limb. According to our model, the subset of of older spot groups will exhibit a $\dot{\theta}$ vs. θ distribution with a smaller $\dot{\theta} = 0$ intercept. The chief difficulty in this procedure, assuming age-determination can be made, may lie in the dirth of older spot-groups. Our Monte Carlo simulation assumed that spot groups had ages exponentially distributed with a mean of three days. Under this assumption, there could be subset of spot groups whose age is arbitrarily large; this is unlikely to be reflected in real data. Moreover, it is likely that a spot group in the advanced stages of decay will not be well modeled as a thin flux tube, as assumed by our model.

Recent models of the solar dynamo (Choudhuri, Schüssler, and Dikpati, 1995; Durney, 1995, 1997; Dikpati and Charbonneau, 1999; Nandy and Choudhuri, 2001) revive the Babcock-Leighton idea that the decay of tilted active regions provides an important ingredient in the dynamo process. Hence, more information on the structure of magnetic fields below the tilted active regions will be extremely valuable for developing more realistic models of the solar dynamo. We hope that in future the observational data of orientational relaxation of bipolar active regions will be analyzed more exhaustively and that our work will provide a framework for extracting useful information from the data.

Acknowledgements

We thank Bob Howard for valuable discussions, and for valuable comments on the manuscript. ARC is immensely grateful to the Solar Physics Group of Montana State University for offering a visiting professorship during the summer of 2000, when this work was initiated. This work was supported under NASA grant NAG5-6110.

Appendix

A. Monte Carlo Simulations

A.1. Initial conditions

The tilt-angle relaxation in our model follows from the initial condition functions $Y^{(\mathrm{c})}(s)$ and $Y^{(\mathrm{t})}(s)$ introduced in Section 3.2. In principle, these functions are determined by following the flux tube dynamics through the rise phase. To illustrate the basic properties of our model, we propose, instead, a simple model of these functions intended to capture their salient features.

The effect of the Coriolis force is captured in the function $Y^{(c)}(s)$ which can be obtained from (12). The right hand side of (12) involves the downflow velocity from the rising flux tube. Once the tube is fully emerged, we expect that the horizontal displacement decreases from its maximum at the solar surface to zero at the base of the convection zone. Based on this reasoning, and the boundary condition (27), we propose a Gaussian

$$Y^{(c)}(s) \;=\; -\frac{1}{2}\sin\lambda\,\Delta x\Theta_0\,e^{-(s/L)^2} \quad , \tag{57}$$

where L is the distortion scale, taken hereafter to be 150 Mm. According to (29), the mean tilt angle for a data set with varying ages t will be

$$\langle\theta\rangle \;=\; |\sin\lambda|\Theta_0\,\langle e^{-(v_{\rm A}t/L)^2}\rangle \quad . \tag{58}$$

Setting this equal to the mean tilt angle $\theta_{\rm J}(\lambda) = 15^\circ\,|\sin(\lambda)|$ found from observation (Fisher, Fan, and Howard, 1995) sets the amplitude

$$\Theta_0 \;=\; \frac{0.262}{\langle e^{-(v_{\rm A}t/L)^2}\rangle} \quad , \tag{59}$$

where the average in the denominator depends on the distribution of ages in the sample.

The turbulent distortion $Y^{(t)}(s)$ should be a random function structured on the spatial scale of the convection zone turbulence. The uppermost portions of the flux tube will have encountered the most turbulence so we expect the distortion amplitudes to be greatest there. We propose the form

$$Y^{(t)}(s) \;=\; e^{-(s/w)^2}\sum_k f_k\,e^{iks} \quad , \tag{60}$$

where the Gaussian envelope function has a width w defining the region of greatest distortion. The Fourier coefficients f_k are uncorrelated, random numbers with $\langle f_k\rangle = 0$. To satisfy the boundary condition (27) each $f_k = f_{-k}$ must be purely real. From (28), the turbulent contribution to the tilt angle is

$$\theta \;=\; -\,4\Delta x^{-1}\,e^{-(v_{\rm A}t/w)^2}\sum_{k>0} f_k\,\cos(kv_{\rm A}t), \tag{61}$$

which is a random variable with the statistics

$$\langle\theta\rangle \;=\; 0 \quad , \quad \langle\theta^2\rangle \;\simeq\; 8\Delta x^{-2}\,\langle e^{-2(v_{\rm A}t/w)^2}\rangle\sum_{k>0}\langle f_k^2\rangle \quad , \tag{62}$$

where $\langle\cos^2(kv_{\rm A}t)\rangle \simeq 1/2$. Simulations of turbulent flux tube distortion (Longcope and Fisher, 1996) show a fairly flat spectrum out to the inverse of the mixing length ℓ, where the spectrum falls of steeply. To resemble this, we set the spectrum to

$$\langle f_k^2\rangle^{1/2} \;=\; 8^{-1/2}\,\Delta x\,\Delta\Theta_0\,\sqrt{\ell\Delta k/2\pi} \quad , \quad |k| \le 2\pi/\ell \quad , \tag{63}$$

where Δk is the spacing between wavenumbers. The coefficient $\Delta\Theta_0$ can be fixed by setting $\langle\theta^2\rangle^{1/2}$ to the observed tilt-angle spread $\theta_{\rm rms} = 10°$ (Fisher, Fan, and Howard, 1995)

$$\Delta\Theta_0 \;=\; \frac{\theta_{\rm rms}}{\langle e^{-2(v_{\rm A}t/w)^2}\rangle^{1/2}} \;=\; \frac{0.174}{\langle e^{-2(v_{\rm A}t/w)^2}\rangle^{1/2}} \quad , \tag{64}$$

where once again the average in the denominator depends on the distribution of ages in the data set.

For our simulations we take the mixing length from the theoretical value at a depth of 66 Mm: $\ell = 23$ Mm, and the envelope width to be twice this value, $w = 46$ Mm. The Alfvén speed is taken to be 1.3×10^4 cm s^{-1} and the Coriolis distortion length is, as mentioned above, $L = 150$ Mm.

A.2. The synthetic data set

We use the model functions above to generate a synthetic set of tilt-angle data. For a given latitude λ_i and relaxation time t_i, the tilt angle is

$$\begin{aligned}\theta_i \;=\; & \Theta_0\,\sin\lambda_i\,\exp[-(v_{\rm A}t_i/L)^2] \;+ \\ & +\;\sqrt{2}\Delta\Theta_0\,\exp[-(v_{\rm A}t_i/w)^2]\,M^{-1/2}\sum_{j=1}^{M}N_j\cos(jv_{\rm A}t_i\Delta k) \quad ,\end{aligned} \tag{65}$$

where $M = 2\pi/\ell\Delta k$ and N_j are independent normal deviates. The tilt angle change $\dot\theta_i$ is found by differentiating this expression with respect to t_i.

To synthesize a data set, we generate 2000 independent values of the pair θ_i and $\dot\theta_i$. The latitude λ_i is drawn from a uniform random distribution between zero and 30 degrees (due to symmetry there is no need to include southern latitudes).

The distribution of ages t_i is meant to reflect the distribution in the Wilson digitized sunspot survey. We model this as an exponential distribution whose mean, $\tau = 3.0$ days, reflects the average age of a sunspot group. For exponentially distributed ages, the average appearing in each coefficient

$$\langle e^{-(t_i/T)^2}\rangle \;=\; \sqrt{\pi}\,\frac{T}{2\tau}\,e^{(T/2\tau)^2}\,{\rm erfc}(T/2\tau) \quad .$$

This average appears in expression (59) with $T = L/v_{\rm A} = 16$ days, and in (64) with $T = w/\sqrt{2}v_{\rm A} = 3.4$ days. Using these values the amplitudes are

$$\Theta_0 \;=\; 0.278 \;=\; 16° \quad , \quad \Delta\Theta_0 = 0.227 \;=\; 13° \quad ,$$

to make the moments of θ_i in the synthetic data set similar to those in the real data set.

References

Achterberg, A.: 1996. *Astron. Astrophys.* **313**, 1008.
Caligari, P., F. Moreno-Insertis, and M. Schüssler: 1995. *Astrophys. J.* **441**, 886.

Choudhuri, A. R.: 1989. *Solar Phys.* **123**, 217.
Choudhuri, A. R. and M. Dikpati: 1999. *Solar Phys.* **184**, 61.
Choudhuri, A. R. and P. A. Gilman: 1987. *Astrophys. J.* **316**, 788.
Choudhuri, A. R., M. Schüssler, and M. Dikpati: 1995. *Astron. Astrophys.* **303**, L29.
Dikpati, M. and P. Charbonneau: 1999. *Astrophys. J.* **518**, 508.
D'Silva, S. and A. R. Choudhuri: 1993. *Astron. Astrophys.* **272**, 621.
D'Silva, S. and R. F. Howard: 1993. *Solar Phys.* **148**, 1.
Durney, B. R.: 1995. *Solar Phys.* **160**, 213.
Durney, B. R.: 1997. *Astrophys. J.* **486**, 1065.
Fan, Y., G. H. Fisher, and E. E. DeLuca: 1993. *Astrophys. J.* **405**, 390.
Fan, Y., G. H. Fisher, and A. N. McClymont: 1994. *Astrophys. J.* **436**, 907.
Hale, G. E., F. Ellerman, S. B. Nicholson, and A. H. Joy: 1919. *Astrophys. J.* **49**, 153.
Howard, R. F.: 1992. *Solar Phys.* **137**, 205.
Howard, R. F.: 1996. *Solar Phys.* **169**, 293.
Howard, R. F., P. A. Gilman, and P. I. Gilman: 1984. *Astrophys. J.* **283**, 373.
Longcope, D. W. and G. H. Fisher: 1996. *Astrophys. J.* **458**, 380.
Lundquist, L. L.; Fisher, G. H.: 2001. *AGU, Sping Meeting 2001.*
Moreno-Insertis, F., M. Schuessler, and A. Ferriz-Mas: 1996. *Astron. Astrophys.* **312**, 317.
Nandy, D. and A. R. Choudhuri: 2001. *Astrophys. J.* **551**, 576.
Press, W. H., B. P. Flannery, S. A. Teukolsky, and W. T. Vetterling: 1986, *Numerical Recipes: The art of scientific computing.* Cambridge: Cambridge University Press.
Ryutov, D. A. and M. P. Ryutova: 1976. *Sov. Phys. JETP* **43**(3), 491.
Spruit, H. C.: 1974. *Solar Phys.* **34**, 277.
Spruit, H. C.: 1981. *Astron. Astrophys.* **98**, 155.
Spruit, H. C., A. M. Title, and A. A. van Ballegooijen: 1987. *Solar Phys.* **110**, 115.
Wang, Y.-M., A. G. Nash, and J. Sheeley, N. R.: 1989. *Astrophys. J.* **347**, 529.
Wang, Y.-M. and J. Sheeley, N. R.: 1989. *Solar Phys.* **124**, 81.